Engineering Fracture Mechanics 259 (2022) 108136

Contents lists available at ScienceDirect

Engineering Fracture Mechanics

journal homepage: www.elsevier.com/locate/engfracmech

Effects of defects on fatigue behavior of TC17 titanium alloy for compressor blades: Crack initiation and modeling of fatigue strength

Weiqian Chi [a], Wenjing Wang [a,*], Wei Xu [b], Gen Li [c], Xin Chen [b], Chengqi Sun [c,d,*]

[a] Key Laboratory of Vehicle Advanced Manufacturing, Measuring and Control Technology (Beijing Jiaotong University), Ministry of Education, Beijing 100044, China
[b] Key Laboratory of Aeronautical Materials Testing and Evaluation, Aero Engine Corporation of China, Beijing Key Laboratory of Aeronautical Materials Testing and Evaluation, Beijing Institute of Aeronautical Materials, Beijing 100095, China
[c] State Key Laboratory of Nonlinear Mechanics, Institute of Mechanics, Chinese Academy of Sciences, Beijing 100190, China
[d] School of Engineering Science, University of Chinese Academy of Sciences, Beijing 100049, China

ARTICLE INFO

Keywords:
TC17 titanium alloy
Surface defect
Very high cycle fatigue
Crack initiation
Fatigue strength prediction

ABSTRACT

S-N data of TC17 titanium alloy with surface defects exhibits plateau region (10^5-10^9 cycles) feature. The effects of defects are greatly related to the defect size. When the defect size is bigger than the critical one, the crack initiates from the defect, and the fatigue strength σ_w incorporating the effects of defects could be expressed as $\sigma_w = C(\sqrt{area})^n$, in which $\sqrt{area}$ denotes the square root of the projection area of defect perpendicular to the principal stress direction, C and n are parameters. The model is also validated by the experimental results of metallic materials in literature.

1. Introduction

Titanium alloys have been widely used in compressor blade of aero-engines due to their excellent mechanical performance such as high strength, high temperature resistance, and corrosion resistance [1]. The compressor blades subject to exceeding 10^7 or even 10^{10} fatigue loadings due to the high inertia centrifugal force and airflow, which might result in fatigue damage and fracture in service [2,3]. The fatigue beyond 10^7 loading cycles (i.e. very high cycle fatigue, VHCF) challenges the traditional fatigue limit concept defined at 10^7 loading cycles [4] and has drawn great attention in recent tens of years, such as for titanium alloys [5–8], steels [9–12], AlSi10Mg alloy [13] and aluminum alloy [14]. For example, Jiao et al. [5] conducted a VHCF test on a TC17 titanium alloy, and the results indicated that the S-N of the TC17 alloy exhibited a continuously descending shape. Liu et al. [15] investigated the effects of stress ratio on high cycle and VHCF behavior of a Ti-6Al-4 V alloy. It was observed that the fracture surface of specimens presented three types of crack initiation mode. For surface-with-facet and interior-with-facet modes, the fatigue strength decreased sharply in VHCF regime. Huang et al. [1,6] showed that the fracture surface of TC17 titanium alloy presented a fine granular area feature at the crack initiation zone in VHCF regime and the crack initiation was due to the H.C.P planar slips of the primary alpha grains.

* Corresponding authors at: State Key Laboratory of Nonlinear Mechanics, Institute of Mechanics, Chinese Academy of Sciences, Beijing 100190, China (C. Sun); Key Laboratory of Vehicle Advanced Manufacturing, Measuring and Control Technology (Beijing Jiaotong University), Ministry of Education, Beijing, 100044, China (W. Wang).
E-mail addresses: wjwang@bjtu.edu.cn (W. Wang), scq@lnm.imech.ac.cn (C. Sun).

https://doi.org/10.1016/j.engfracmech.2021.108136
Received 25 May 2021; Received in revised form 18 November 2021; Accepted 20 November 2021
Available online 25 November 2021

The actual components, such as the compressor blades, usually inevitably contain defects during the casting and forging process [16] or caused by impacts of debris ingested by aero-engine in service [17,18]. The defects might greatly decrease the fatigue performance of metallic materials. For instance, it has been found that the larger the defect size, the lower the fatigue life of the S38C steel [19], EA4T steel [20,21], martensitic stainless steel [22], Ni-based superalloy 718 [23], and selective laser melted Ti-6Al-4 V alloy [24,25]. Especially, Murakami [26] investigated the effect of small defects on the fatigue strength (at 10^7 cycles) of metallic materials, and proposed a $\sqrt{area}$ model to correlate the fatigue strength, defect size and the threshold value of the crack propagation, in which $\sqrt{area}$ is the square root of the projection area of the defect perpendicular to the principle stress direction. The $\sqrt{area}$ model or the concept of $\sqrt{area}$ is then widely used or developed to investigate the fatigue performance of metallic materials with defects [19–24,27,28].

TC17 titanium alloy is one of the most important materials used for compressor blades in aero-engines. Therefore, it is significant to clarify the influence of defects on the fatigue behavior of TC17 titanium alloy, which is of great help in the design of the aero-engine and the safety of the aircraft. In this paper, rotating bending fatigue tests are at first performed for the high cycle and VHCF behavior of the TC17 titanium alloy with and without surface defects. Then, the effects of defects on both the crack initiation and fatigue performance of the TC17 titanium alloy are investigated. The microstructure characteristic in the crack initiation and early growth region is observed by using scanning electron microscope (SEM), electron backscatter diffraction (EBSD) and transmission Kikuchi diffraction (TKD) with the help of the focused ion beam (FIB) technique and the argon ion polishing. Finally, a model based on the concept of $\sqrt{area}$ is developed to correlate the defects and fatigue strength in VHCF regime. The model is also used to correlate the effects of defects or crack on the fatigue strength of some metallic materials in high cycle fatigue regime in literature.

2. Materials and methods

2.1. Materials

The material used in the paper is a TC17 titanium alloy with chemical compositions 4.97 Al, 4.19 Cr, 1.90 Zr, 4.12 Mo, 2.09 Sn, 0.11O, <0.10 Fe, 0.0052H, 0.004C and balanced Ti in weight percent. The beta forging is at first for the material. Then, the material is under solid solution at 800 °C for 4 h and cooled by water, and finally under the aging treatment at 620 °C for 8 h. The specimens are

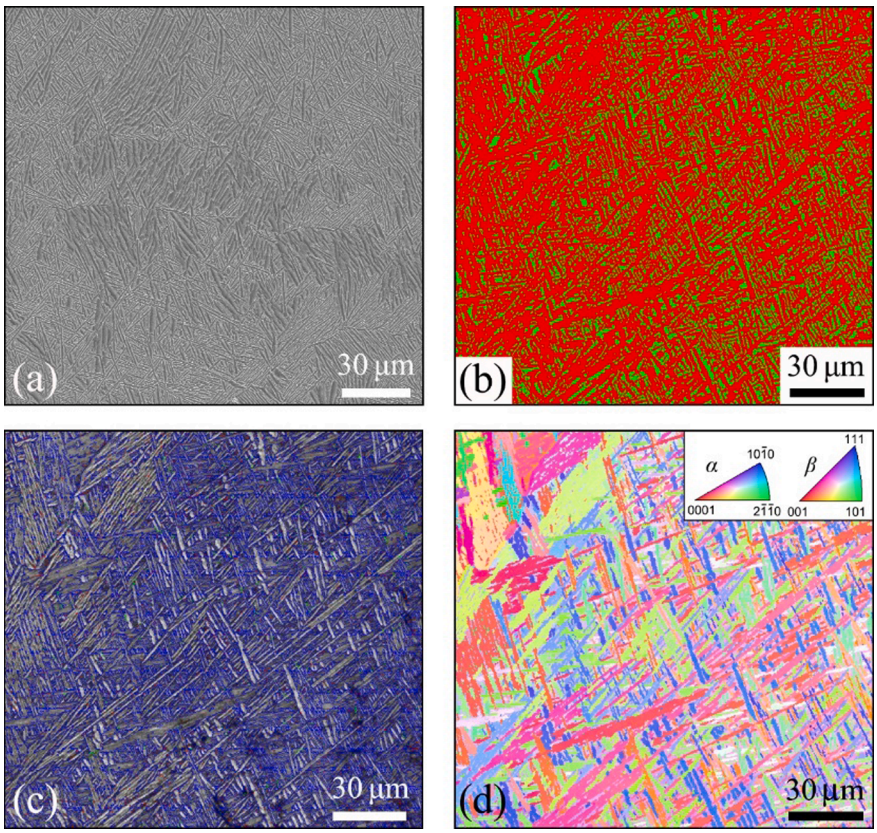

Fig. 1. Microstructure of the present TC17 titanium alloy. (a) Secondary electron image; (b) Phase distribution, red color: alpha phase, green color: beta phase; (c) Grain boundary map, red lines: misorientation between 2° and 5°, green lines: misorientation between 5° and 15°, blue lines: misorientation between 15° and 180°; (d) Orientation distribution map by inverse pole figure.

cut from the solid bar after heat treatment. Fig. 1a–d show the secondary electron image, phase map, grain boundary map and EBSD inverse pole figure (IPF) for the microstructure of the present TC17 titanium alloy. It is basketweave structure. The β phase is between the lamellar α phase, and the secondary α-phase is distributed on the β-matrix. The tensile strength is 1145 MPa and the yield strength is 1061 MPa, which are obtained from two cylindrical specimens with diameter of 5 mm and gauge length of 30 mm by the servo-hydraulic test system.

2.2. Fatigue tests

All the fatigue tests are performed on a rotating bending machine at room temperature in air. The frequency is 50 Hz and the stress ratio R is –1. Five types of specimens are used. One is smooth specimen (Fig. 2a), and the other four are specimens with different surface defects, i.e. defect-A, defect-B, defect-C and defect-D in Fig. 2b–e. The defects are manufactured in the smallest section of the smooth specimen (Fig. 2a) by a small drill. The approximate shape and dimension of defects are shown in Fig. 2b–e, which refers to the SEM pictures of the defect on the fracture surface. The width w for defect-A is related to the depth h of the defect due to that the depth of defect-A is very shallow. The elastic stress concentration factor is 1.02 for the smooth specimen, which is defined as the ratio of the maximum principal stress at the notch root to that of the cylindrical specimen with the same minimum diameter under the identical loading condition. The surfaces of the hourglass part are ground and polished for both the smooth specimens and the specimens before the defects are drilled.

2.3. Observation methods

The fracture surfaces of failed specimens are observed by SEM. For typical crack initiation regions, cross-section samples parallel to the axial direction of the specimen are prepared by FIB technique and then observed by SEM, EBSD and TKD. The cross-section sample perpendicular to the axial direction of the specimen is also prepared for the defect region by grinding and argon ion polishing, and then observed by EBSD. During the cutting process by FIB, a thin coating layer of platinum is used to protect the fracture surface of the cross-section sample.

3. Experimental results and analyses

3.1. Fatigue performance of smooth specimens and specimens with surface defects

Fig. 3 shows the results of S-N data for the smooth specimens and the specimens with different surface defects, in which the nominal stress for the specimens with surface defects is calculated by the smallest section of the specimens before the defects are drilled. The original experimental data are given in Tables 1–3.

It is seen from Fig. 3 that, when the fatigue strength is in terms of the nominal stress, the surface defect has a substantial influence on the fatigue strength of the TC17 alloy, and the fatigue strength decreases with an increase of the defect size. For instance, the fatigue strength at 10^8 cycles of the specimens with defect-B, defect-C and defect-D is 11%, 29%, and 39% lower than that of smooth specimens, respectively. Here, the fatigue strength at 10^8 cycles is determined by the average of the minimum fatigue strength of the specimens failed before 10^8 cycles and the maximum fatigue strength of the specimens not failed after 10^8 cycles.

Fig. 3 also shows that the S-N data of the TC17 alloy has the feature of plateau region for both the smooth specimens and specimens with surface defects. This plateau region is between about 10^7-10^9 cycles for the smooth specimen and is between about 10^5-10^9 cycles

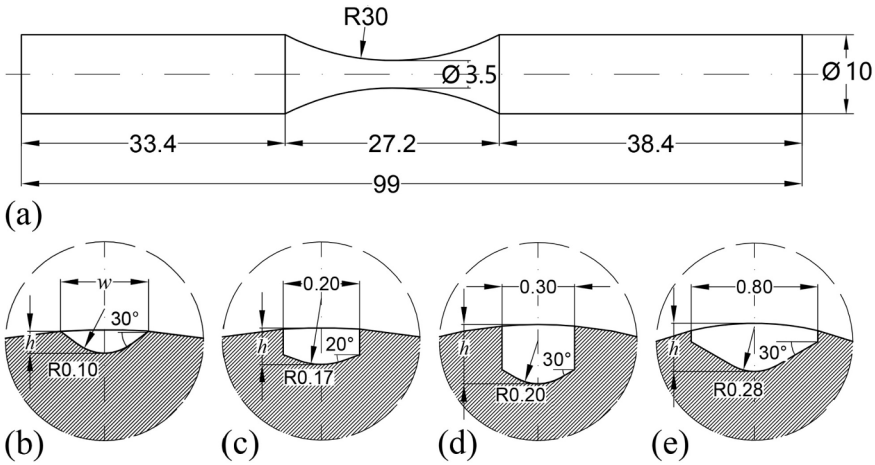

Fig. 2. Shape and dimension of specimens (in mm). (a) Smooth specimen; (b)-(e) Sketch maps for the cross-section of defect-A, defect-B, defect-C and defect-D, respectively.

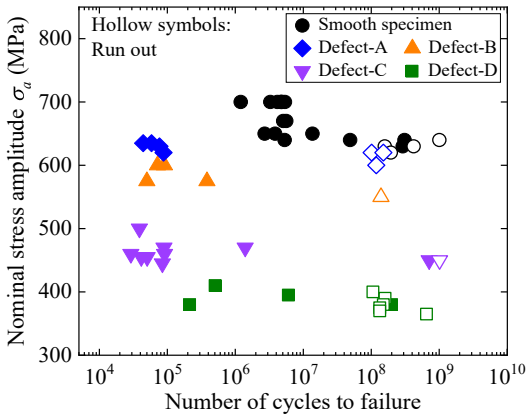

Fig. 3. S-N data of smooth specimens and specimens with surface defects.

Table 1
Nominal stress amplitude σ_a, fatigue life N_f and crack initiation site for smooth specimens.

σ_a (MPa)	N_f	Crack initiation site	σ_a (MPa)	N_f	Crack initiation site
700	1.20×10^6	Surface	640	4.90×10^7	Surface
700	3.29×10^6	Surface	640	3.09×10^8	Surface
700	4.16×10^6	Surface	630	2.91×10^8	Interior
700	4.64×10^6	Surface	640*	1.01×10^9	
700	4.80×10^6	Interior	630*	1.58×10^8	
700	4.85×10^6	Interior	630*	4.20×10^8	
700	5.38×10^6	Interior	620*	1.94×10^8	
670	5.07×10^6	Surface			
670	5.63×10^6	Surface			
650	2.71×10^6	Surface			
650	3.85×10^6	Interior			
650	1.37×10^7	Surface			
640	5.32×10^6	Surface			

* It denotes that the specimen is unbroken.

Table 2
Nominal stress amplitude σ_a, fatigue life N_f and defect size $\sqrt{area}$ for specimens with surface defect-A and defect-B, respectively.

Specimens with surface defect-A			Specimens with surface defect-B		
σ_a (MPa)	N_f	$\sqrt{area}$ (μm)	σ_a (MPa)	N_f	$\sqrt{area}$ (μm)
635	4.41×10^4	84	600	9.08×10^4	145
635	5.84×10^4	82	600	7.17×10^4	186
630	7.66×10^4	76	575	4.99×10^4	139
620	8.79×10^4	75	575	3.83×10^5	143
620*	1.51×10^8	73	550*	1.39×10^8	174
620*	1.01×10^8				
600*	1.19×10^8				

* It denotes that the specimen is unbroken, and the associated defect size is obtained from the fracture surface by a following higher stress amplitude.

for the specimens with defects. This indicates that, for both the smooth specimens and specimens with surface defects, the fatigue strength of the TC17 alloy does not decrease with the increase of the fatigue life in VHCF regime.

3.2. SEM observation of fracture surface

Fig. 4 shows the fracture surface morphologies of several smooth specimens failed in high cycle and VHCF regimes. The crack initiation sites of the failed smooth specimens are shown in Table 1. SEM observations indicate that the smooth specimens fail from the specimen surface (Fig. 4b and 4d) or the specimen interior (Fig. 4f and 4h) for both the high cycle and VHCF of the TC17 alloy. For the crack initiates from the interior of the specimen, the fracture surface exhibits “fine granular area” like feature in the crack initiation origin, as shown in Fig. 4f. In contrast to the smooth specimens, the fatigue cracks all initiate from the defects for the specimens with

Table 3
Nominal stress amplitude σ_a, fatigue life N_f and defect size $\sqrt{area}$ for specimens with surface defect-C and defect-D, respectively.

Specimens with surface defect-C			Specimens with surface defect-D		
σ_a (MPa)	N_f	$\sqrt{area}$ (μm)	σ_a (MPa)	N_f	$\sqrt{area}$ (μm)
500	3.88×10^4	270	410	5.06×10^5	354
470	8.94×10^4	251	395	6.04×10^6	340
470	1.40×10^6	287	380	2.12×10^5	317
460	2.91×10^4	249	380	1.99×10^8	317
460	9.10×10^4	247	400*	1.06×10^8	294
455	4.13×10^4	248	390*	1.60×10^8	307
455	5.04×10^4	287	380*	1.51×10^8	291
450	7.13×10^8	233	375*	1.34×10^8	296
445	8.45×10^4	281	370*	1.33×10^8	362
450*	1.01×10^9	248	365*	6.50×10^8	

* It denotes that the specimen is unbroken, and the associated defect size is obtained from the fracture surface by the following higher stress amplitude.

surface defects. The morphologies of the fracture surface for specimens with different surface defects are shown in Fig. 5.

4. Discussion

4.1. SEM and EBSD observation of extracted samples in crack initiation region

It is shown in Section 3.2 that the crack initiation region presents "fine granular area" like feature for the interior crack initiation of smooth specimens. Here, the cross-section sample parallel to the axial direction of the specimen is prepared by using FIB technique, and the microstructure characteristic beneath the "fine granular area" like region is observed by SEM and TKD.

Fig. 6 shows the SEM and TKD results of the cross-section sample extracted at the "fine granular area" like region in Fig. 4h. It is seen from Fig. 6b and c that there are refined grains for the microstructure beneath the "fine granular area" like region. The grain refinement phenomenon is also observed for the microstructure beneath the fine granular area or rough area for Ti-6Al-4 V and VT3-1 titanium alloys [29–31]. The Kernel average misorientation (KAM) map in Fig. 6b and d shows that the plastic deformation is more significant in the α grain where the grain refinement occurs. This indicates that the formation of refined grains is related to the high strain localization caused by microstructure inhomogeneity or deformation incompatibility [31].

In order to understand the microstructure around the defects, Fig. 7 shows the EBSD observations for the cross-section samples parallel to the axial direction of the specimen (Fig. 7a) and the one perpendicular to the axial direction of the specimen (Fig. 5f). The cross-section sample parallel to the axial direction of the specimen is prepared by FIB technique. The cross-section sample perpendicular to the axial direction of the specimen is prepared by grinding and then argon ion polishing. The IPF and KAM image in Fig. 7 indicate that the microstructure in the vicinity of the defects has no clear difference with the microstructure of the bulk material. Fig. 7b also indicates that there is no grain refinement phenomenon beneath the fracture surface in the crack initiation and early growth region. This result is similar to that observed for the VHCF of a structural steel failed from the surface defect [32].

4.2. Finite element analysis for the effects of defects

The result in Fig. 3 indicates that the surface defect might lead to a substantial decrease in fatigue strength when the fatigue strength is in terms of the nominal stress. Here, the stress distribution around the defect is at first analyzed by finite element analysis and by the assumption that the material is uniform and isotropic. The elastic stress concentration factor is defined as the maximum principal stress at the defect to that of the column specimen with the same smallest section of the specimen before the defect is drilled. The shapes of defects modeled in the calculation are as those illustrated in Fig. 2b–e. The values of w and h are measured by Image-Pro Plus (IPP) software on SEM pictures of the fracture surface. As an example, Fig. 8 shows the finite element model and stress distribution of the specimen with the surface defect-C subjected to a concentrated load of 15 N along the negative direction of y axis. The load point is 9.44 mm away from the left end of the specimen in Fig. 8a (i.e. Fig. 2a). The tetrahedral elements (C3D10M type) are taken, and refinement meshes (the mesh size is 10 μm) are used for the region around the defect.

Table 4 shows the elastic stress concentration factor calculated for the specimens with different surface defects. It is seen from Table 4 that, the elastic stress concentration factor is about 2.0 for the specimens with defect-A and defect-D, and is about 2.5 for the specimens with defect-B and defect-C. So, when the fatigue strength is in terms of the local stress instead of the nominal stress in Fig. 2b, the fatigue strength of specimens with surface defects is higher than that of the smooth specimens at the same fatigue life in VHCF regime, namely that the peak-stress method [33] cannot be effectively used to correlate the effects of surface defects on the fatigue strength of the present TC17 alloy.

4.3. Model for effects of defects on fatigue strength

It has been shown that the defect size $\sqrt{area}$ (square root of the projection area of the defect perpendicular to the principal stress

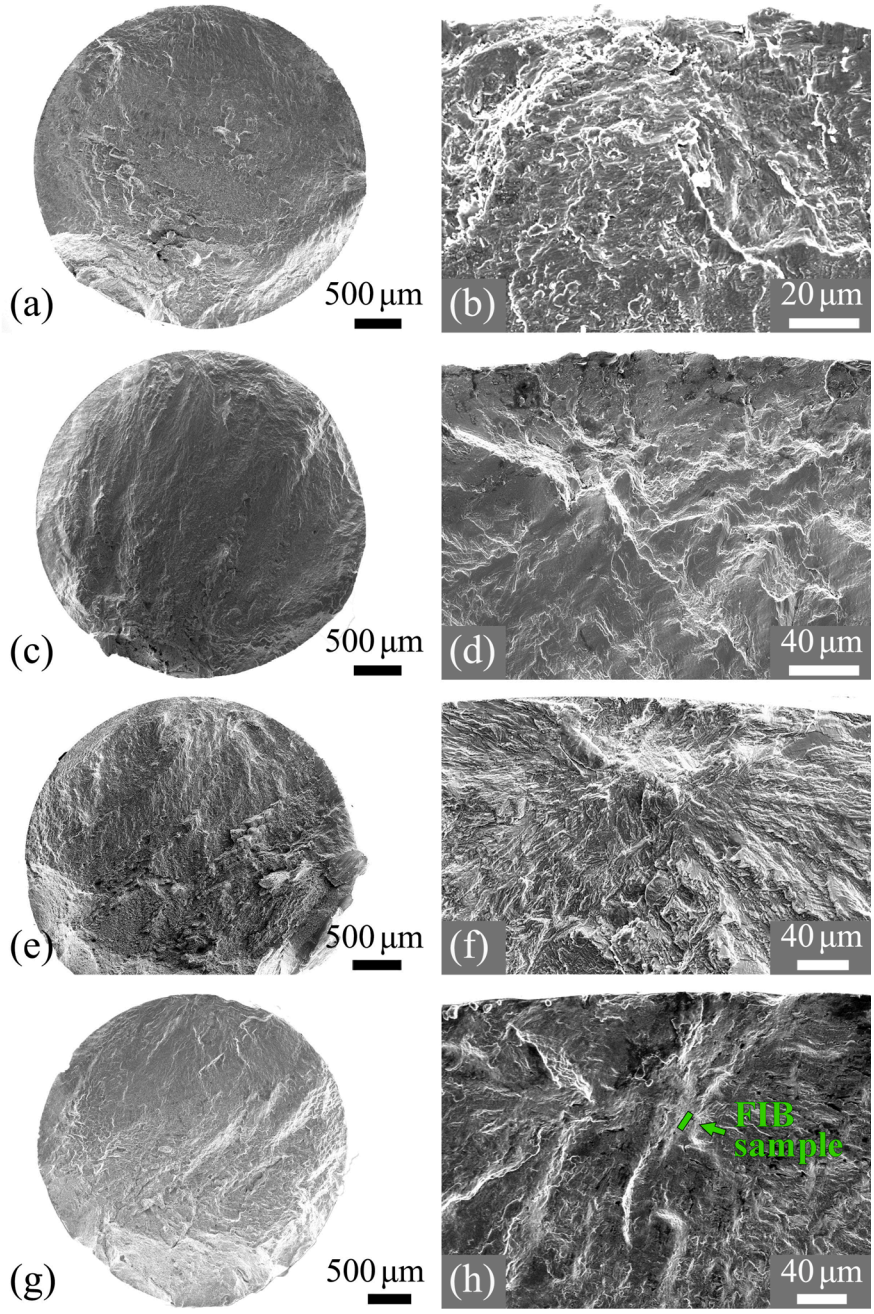

Fig. 4. SEM images of fracture surfaces for smooth specimens. (a) and (b): crack initiation from specimen surface, $\sigma_a = 700$ MPa, $N_f = 4.16 \times 10^6$; (c) and (d): crack initiation from specimen surface, $\sigma_a = 640$ MPa, $N_f = 4.90 \times 10^7$; (e) and (f): crack initiation from specimen interior, $\sigma_a = 700$ MPa, $N_f = 4.85 \times 10^6$; (g) and (h): crack initiation from specimen interior, $\sigma_a = 630$ MPa, $N_f = 2.91 \times 10^8$; (a), (c), (e) and (g) are images of the whole fracture surface, (b), (d), (f) and (h) are the magnified images of the region including the crack initiation site. The short line in (h) denotes the location where the sample along the axial direction of the specimen is extracted for TKD observation.

direction) is a good parameter in correlating the influence of defects on fatigue strength of steels in some cases [26]. Here, the defect sizes of the specimens are measured from the SEM images by IPP software, and shown in Tables 2 and 3. Combined with the defect sizes in Tables 2 and 3, there exists a critical defect size, when the defect size is bigger than the critical one, the larger the defect size, the more notable decrease the fatigue strength in Fig. 3. So, it is thought that the fatigue strength and the defect size have the following form in VHCF regime:

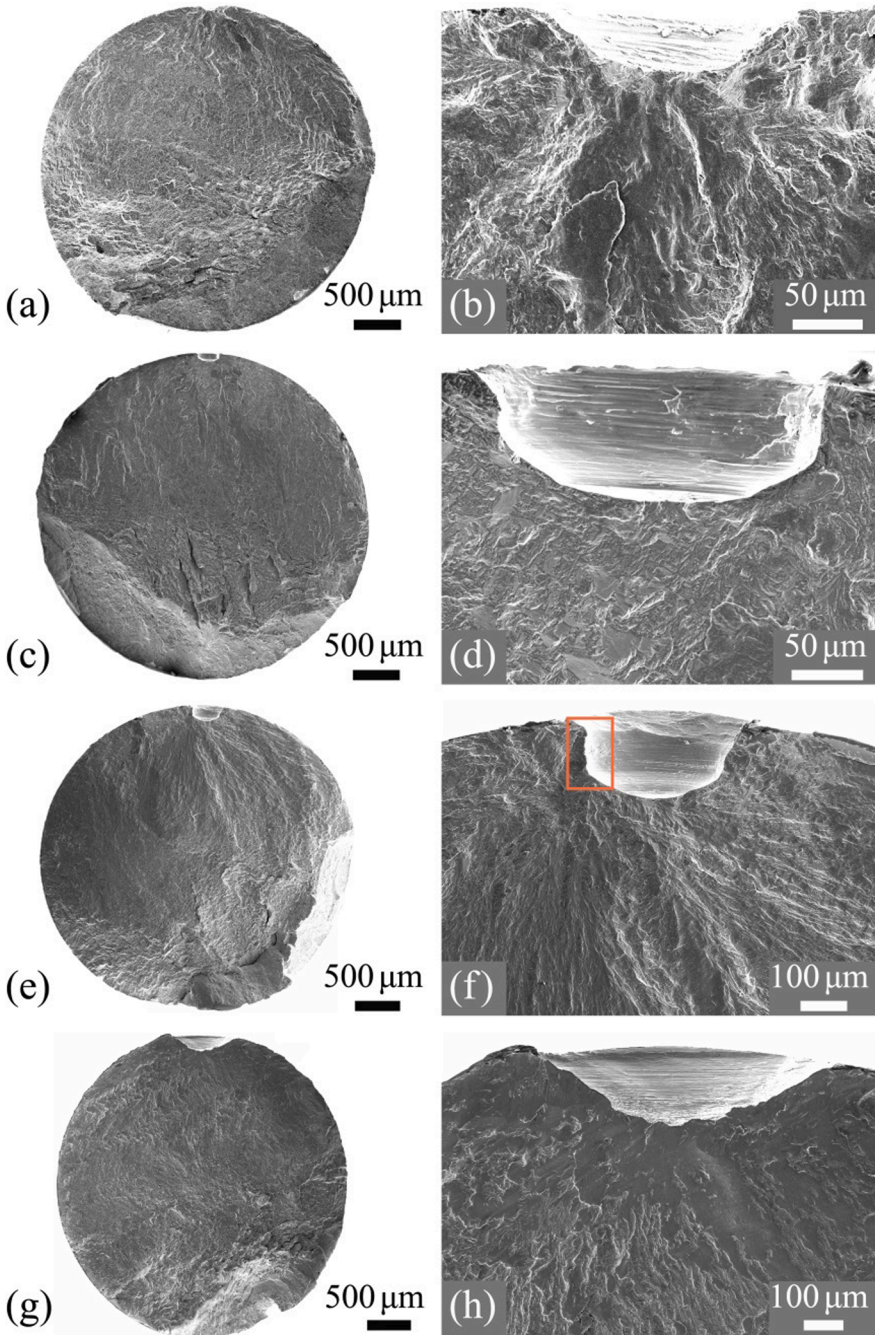

Fig. 5. SEM images of fracture surfaces for specimens with surface defects. (a) and (b): Defect-A, $\sigma_a = 620$ MPa, $N_f = 8.79 \times 10^4$; (c) and (d): Defect-B, $\sigma_a = 575$ MPa, $N_f = 4.99 \times 10^4$; (e) and (f): Defect-C, $\sigma_a = 450$ MPa, $N_f = 7.13 \times 10^8$; (g) and (h): Defect-D, $\sigma_a = 380$ MPa, $N_f = 1.99 \times 10^8$. (a), (c), (e) and (g) are images of the whole fracture surface; (b), (d), (f) and (h) are the magnified images of the region including the crack initiation site. The orange rectangular in (f) denote the region for EBSD observation after polished.

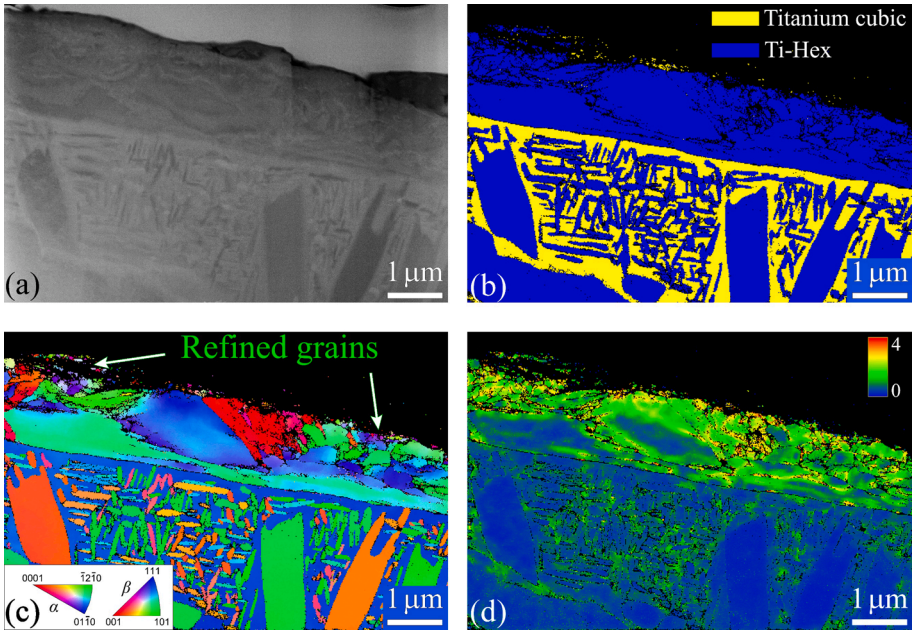

Fig. 6. SEM and TKD results of the extracted cross-section sample in Fig. 4h. (a): SEM image of the cross-section sample for TKD observation; (b): Phase distribution, blue color: alpha phase, yellow color: beta phase; (c): Orientation distribution map by IPF; (d): KAM map.

$$\sigma_w = \begin{cases} C\left(\sqrt{area}\right)^n & for \quad \sqrt{area} \geq \sqrt{area_0} \\ \sigma_{w,0} & for \quad \sqrt{area} < \sqrt{area_0} \end{cases} \tag{1}$$

i.e.

$$\log_{10}\sigma_w = \begin{cases} n\log_{10}\sqrt{area} + \log_{10}C & for \quad \sqrt{area} \geq \sqrt{area_0} \\ \log_{10}\sigma_{w,0} & for \quad \sqrt{area} < \sqrt{area_0} \end{cases} \tag{2}$$

where σ_w denotes the fatigue strength of the specimen with defect, $\sigma_{w,0}$ denotes the fatigue strength of the smooth specimen, $\sqrt{area_0} = (\sigma_{w,0}/C)^{1/n}$ denotes the critical size of the defect less than which the defect does not affect the fatigue strength, C and n are parameters of the material, which can be obtained by the least square regression for the value of $\log_{10}\sigma_w$ smaller than $\log_{10}\sigma_{w,0}$ associated with the value of $\log_{10}\sqrt{area}$.

4.3.1. Comparison with present experimental data

Fig. 9 shows the present model for correlating the experimental data of the TC17 alloy. Here, the average defect sizes are used for analysis for each kind of defect in Tables 2 and 3. The fatigue strength at 10^8 cycles is considered, and it is defined as that in Sec. 3.1. The relative errors for the present model to the experimental data are shown in Table 5. It is seen that the present model is well in correlating the influence of defects on the fatigue strength in VHCF regime. The relative errors are within 2.0% for all the experimental data.

4.3.2. Comparison with experimental data in literature

Fig. 10 shows a validation of the present model for correlating the influence of defects on the fatigue strength of steels in literature [19–21]. It is seen from Fig. 10 that the present model is in well agreement with the experimental data for the effects of surface defects on the fatigue strength of S38C steel and EA4T steel in high cycle fatigue regime. Further, Fig. 10 indicates that the effects of defects on the fatigue strength are not only related to the defect size but also the introduced form of the defects. For example, the fatigue strength of the EA4T steel with TB defect size of 568 μm is 340 MPa in Fig. 10c. While for the same fatigue strength of the EA4T steel with IN defect in Fig. 10d, the defect size is 255 μm, which is smaller than the TB defect size

It is also noted that the defect size might be smaller than a certain maximum defect size (i.e. ~ 1000 μm) for the application of the present model [26]. For instance, for the TB defect of S38C axle steel in literature [19], the fatigue strength decreases sharply with increasing the value of $\sqrt{area}$ when $\sqrt{area}$ is bigger than 1000 μm (1300 μm and 1550 μm). The data for the defect size bigger than 1000 μm are not used in Fig. 10a.

Cracks are special defects in some sense. So, the present model is also attempted to correlate the effects of cracks on the fatigue strength. For the specimen with crack, the defect size is instead by the crack length in the present model. Fig. 11 shows the present model for the effects of cracks on the fatigue strength of steels in literature [34–36]. It is seen that the present model gives well correlation for the effects of cracks on the fatigue strength of the 2.25Cr-1Mo steel, 0.22 %C steel and JIS SM41 mild (0.18 %C) steel in

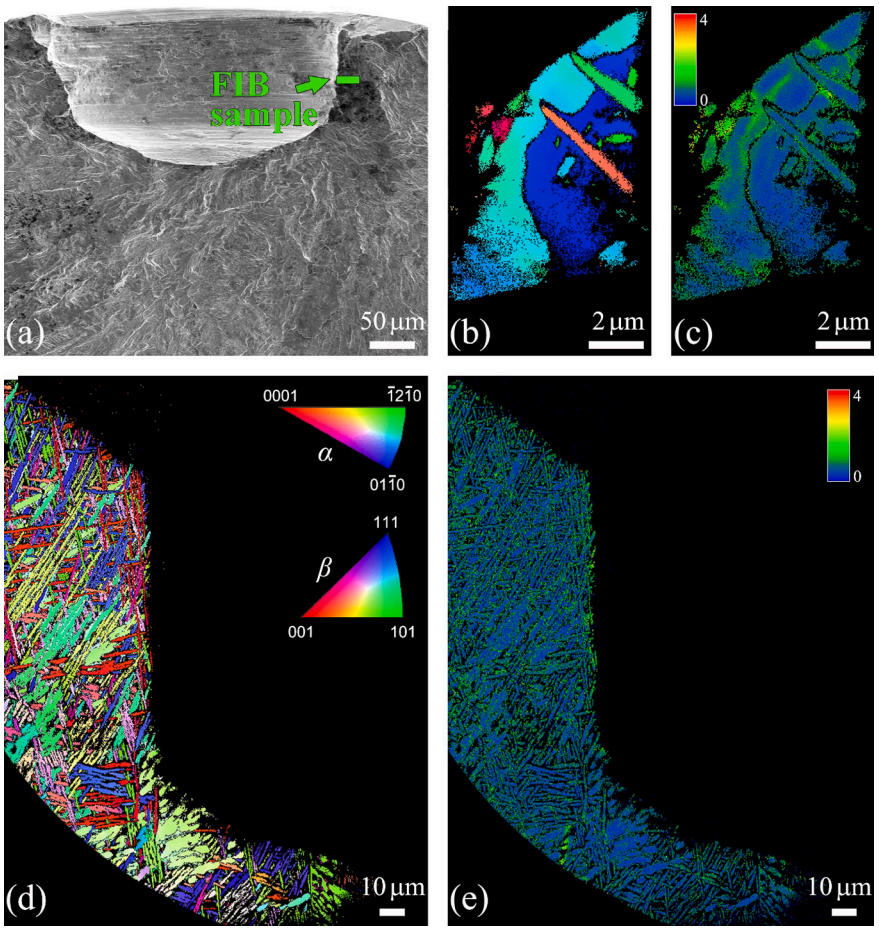

Fig. 7. SEM and EBSD results for the specimen with defect-C, $\sigma_a = 450$ MPa and $N_f = 7.13 \times 10^8$. (a) SEM image for the mated fracture surface of the specimen in Fig. 5f, in which the short line denotes the location of the extracted sample for EBSD observation. (b) and (c): IPF and KAM are images of the extracted sample in (a), respectively. (d) and (e): IPF and KAM images of the cross-section sample in Fig. 5f, respectively.

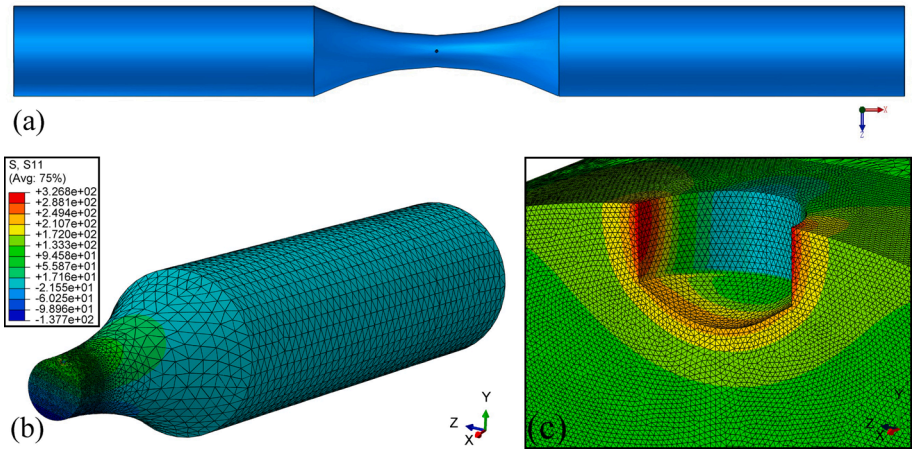

Fig. 8. (a): Model of the specimen with defect-C; (b): Stress distribution under a concentrated load of 15 N along the negative direction of *y* axis; (c): Magnified image of the region near the defect-C in (b).

Table 4
Elastic stress concentration factor for specimens with different surface defects.

	Defect-A	Defect-B	Defect-C	Defect-D
Depth of defect h (mm)	0.04 ~ 0.06	0.09 ~ 0.13	0.19 ~ 0.25	0.23 ~ 0.29
Stress concentration factor	1.89 ~ 1.95	2.26 ~ 2.49	2.44 ~ 2.72	1.91 ~ 1.96

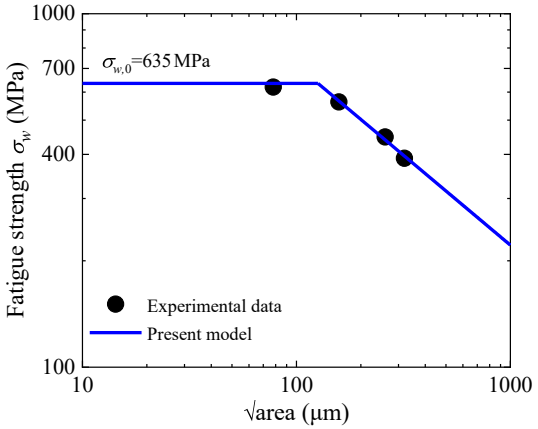

Fig. 9. Comparison of the present model with experimental data for the present TC17 alloy.

Table 5
Comparison of experimental fatigue strengths and the calculated ones by the present model

$\sqrt{area}$ (μm)	Experimental fatigue strength (MPa)	Calculated fatigue strength (MPa)	Relative error (%)
158	563	566	0.53
260	448	440	1.79
320	390	395	1.28

high cycle fatigue regime [34–36].

The present experimental data and the data in literature indicate that the present model is promising in correlating not only the effects of defect size but also the crack length on the fatigue strength of metallic materials. In other words, the present model describes the trends of the fatigue strength with defect size or crack length, and is applicable to predict the fatigue strength of specimens with defects or cracks.

5. Conclusions

In this paper, we investigate the effects of surface defects on high cycle and VHCF behavior of the TC17 titanium alloy used for compressor blades in aero-engines by rotating bending fatigue test. The main results are as follows.

(1) S-N data of the TC17 titanium alloy exhibits the characteristic of plateau region for both the smooth specimen and the specimen with surface defects. For the smooth specimen, the plateau region is between 10^7-10^9 cycles, while for the specimen with surface defects, the plateau region is between 10^5-10^9 cycles.

(2) The effects of defects on the fatigue behavior of TC17 titanium alloy are greatly dependent of the defect size and the introduced form of the defect. There exists a critical size of defect less than which the defect does not affect the fatigue strength and the specimen does not fail from the defect. When the defect size is bigger than the critical size, the crack initiates from the defect, and the fatigue strength is reduced due to the effect of defect.

(3) A model is developed to correlate the effects of defects on the fatigue strength of TC17 titanium alloy in high cycle and VHCF regime, i.e. the fatigue strength σ_w incorporating the effects of defects could be expressed as $\sigma_w = \begin{cases} C(\sqrt{area})^n for\ \sqrt{area} \geq \sqrt{area_0} \\ \sigma_{w,0}\ for\ \sqrt{area} < \sqrt{area_0} \end{cases}$, in which $\sqrt{area}$ denotes the square root of the projection area of the defect perpendicular to the principle stress direction, $\sigma_{w,0}$ denotes the fatigue strength of the smooth specimen, $\sqrt{area_0}$ denotes the critical size of defect less than which the defect does not affect the fatigue strength, C and n are parameters related to fatigue life, material and the introduced form of defect. The model also accords well the experimental data for the effects of defects or cracks on the fatigue strength of metallic materials in high cycle fatigue regime in literature.

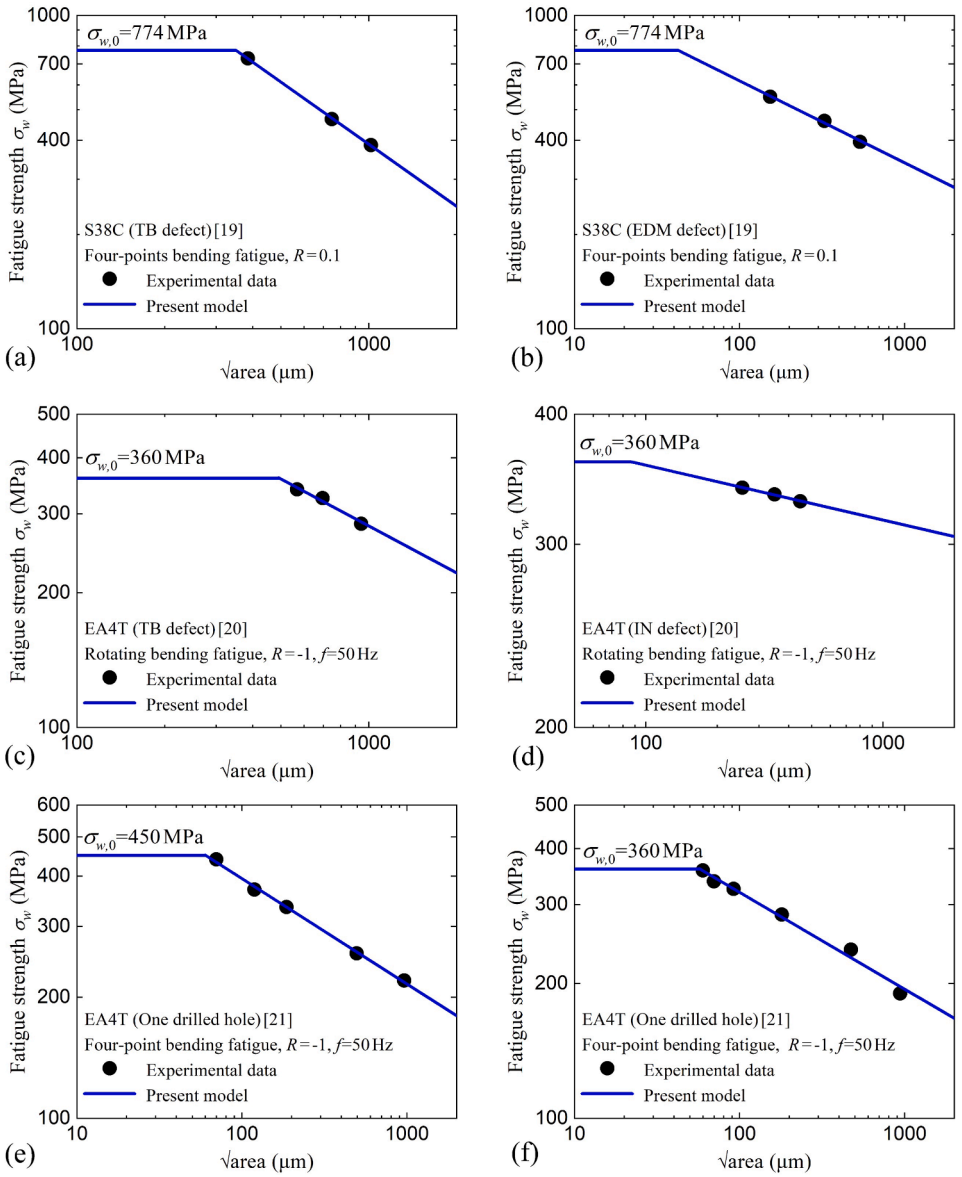

Fig. 10. Present model for correlating the effects of defects on fatigue strength in terms of stress amplitude of steels in literature. (a) S38C steel with defects by a compressed-gas gun with tungsten steel (i.e. TB defect); (b) S38C steel with defects by electronic discharge machine (i.e. EDM defect); (c) EA4T steel with TB defects; (d) EA4T steel with defects by an indenter (i.e. IN defect); (e) EA4T steel (micro-shot peened) with one drilled hole defect; (f) EA4T steel (un-peened) with one drilled hole defect.

The present results are helpful in understanding the fatigue behavior of the TC17 titanium alloy and predicating the fatigue strength of the TC17 titanium alloy with defects. The paper also provides a method for evaluating the influence of defects or cracks on the fatigue strength of metallic materials in high cycle and VHCF regimes.

6. Data Availability

The data are available upon request by contacting with the corresponding author.

CRediT authorship contribution statement

Weiqian Chi: Methodology, Formal analysis, Investigation, Writing – original draft, Writing – review & editing. **Wenjing Wang:** Methodology, Formal analysis, Investigation, Writing – review & editing, Funding acquisition. **Wei Xu:** Conceptualization, Investigation, Writing – review & editing. **Gen Li:** Formal analysis, Writing – review & editing. **Xin Chen:** Formal analysis, Writing – review &

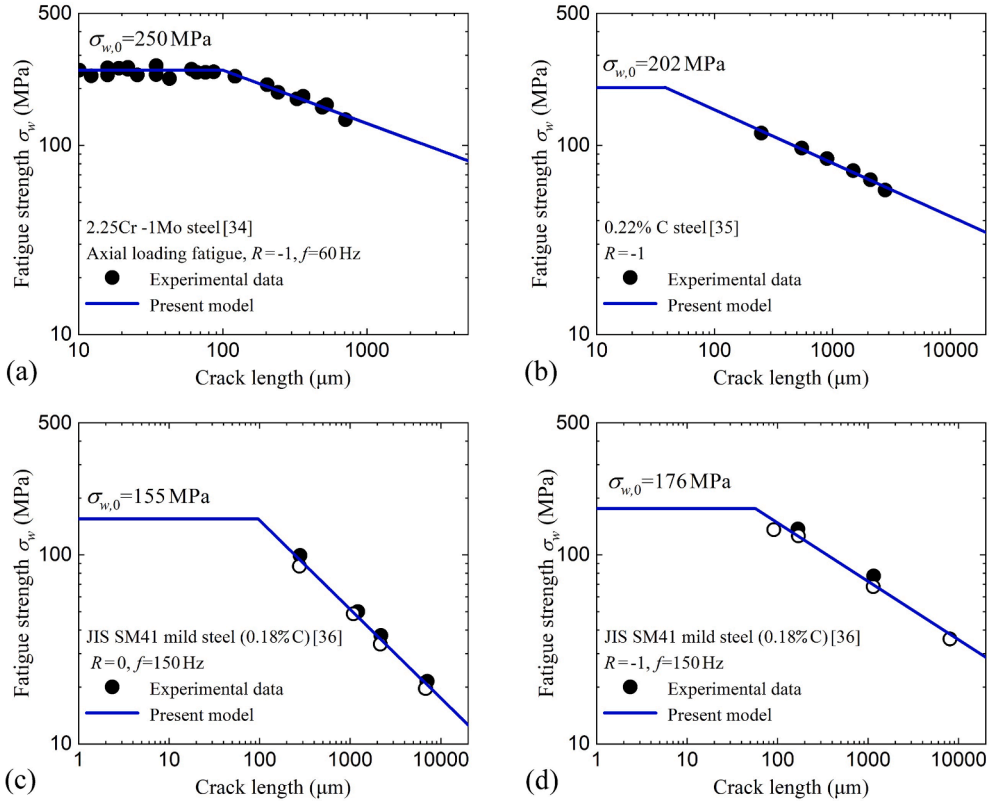

Fig. 11. Present model for correlating the effects of cracks on the fatigue strength in terms of stress amplitude of steels in literature. (a) 2.25Cr-1Mo steel; (b) 0.22 %C steel; (c) and (d) JIS SM41 mild (0.18 %C) steel at R = 0 and R = -1, respectively, in which the solid symbol denotes broken specimens, and the hollow symbol denotes specimens with no growth crack. The fatigue strength for the smooth specimen in (c) and (d) is the average value of the fatigue strength of the broken specimen and that of the specimen with no growth crack extracted from literature [36].

editing. **Chengqi Sun:** Conceptualization, Methodology, Formal analysis, Investigation, Writing – original draft, Writing – review & editing, Funding acquisition, Supervision.

Declaration of Competing Interest

The authors declare that they have no known competing financial interests or personal relationships that could have appeared to influence the work reported in this paper.

Acknowledgements

The authors gratefully acknowledge the support from the National Natural Science Foundation of China (91860112), the National Natural Science Foundation of China Basic Science Center for "Multiscale Problems in Nonlinear Mechanics" (11988102) and Science and Technology Research and Development Program of China State Railway Group Co., Ltd. (P2020J024).

References

[1] Huang ZY, Liu HQ, Wang HM, Wagner D, Khan MK, Wang QY. Effect of stress ratio on VHCF behavior for a compressor blade titanium alloy. Int J Fatigue 2016; 93:232–7.
[2] Shanyavskiy AA. Very-high-cycle-fatigue of in-service air-engine blades, compressor and turbine. Sci. CHINA Physics, Mech. Astron. 2014;57:19.
[3] SHANYAVSKIY A. Fatigue limit – Material property as an opened or closed system? Practical view on the aircraft components failures in GCF area. Int J Fatigue 2006;28(11):1647–57.
[4] Hong Y, Sun C. The nature and the mechanism of crack initiation and early growth for very-high-cycle fatigue of metallic materials - An overview. Theor Appl Fract Mech 2017;92:331–50.
[5] Jiao S, Gao C, Cheng Li, Li X, Feng Yu. A very high-cycle fatigue test and fatigue properties of TC17 titanium alloy. J. Mater. Engng. Perform. 2016;25(3): 1085–93.
[6] Liu H, He C, Huang Z, Wang Q. Very high cycle fatigue failure mechanism of TC17 alloy. Acta Metall Sin 2017;53:1047–54.
[7] Li Y, Song Q, Feng S, Sun C. Effects of loading frequency and specimen geometry on high cycle and very high cycle fatigue life of a high strength titanium alloy. Materials 2018;11:1628.

[8] Xu W, Zhao Y, Chen X, Zhong B, Yu H, He Y, et al. An ultra-high frequency vibration-based fatigue test and its comparative study of a titanium alloy in the VHCF regime. Metals 2020;10:1415.
[9] Cong T, Qian G, Zhang G, Wu S, Pan X, Du L, et al. Effects of inclusion size and stress ratio on the very-high-cycle fatigue behavior of pearlitic steel. Int J Fatigue 2021;142:105958.
[10] Song Q, Sun C. Mechanism of crack initiation and early growth of high strength steels in very high cycle fatigue regime. Mater Sci Eng A 2020;771:138648.
[11] Sakai T, Oguma N, Morikawa A. Microscopic and nanoscopic observations of metallurgical structures around inclusions at interior crack initiation site for a bearing steel in very high-cycle fatigue. Fatigue Fract. Eng Mater Struct 2015;38:1305–14.
[12] Sun C, Song Q, Zhou L, Liu J, Wang Y, Wu X, et al. The formation of discontinuous gradient regimes during crack initiation in high strength steels under very high cycle fatigue. Int J Fatigue 2019;124:483–92.
[13] Zhang W, Hu Y, Ma X, Qian G, Zhang J, Yang Z, et al. Very-high-cycle fatigue behavior of AlSi10Mg manufactured by selected laser melting: Crystal plasticity modeling. Int J Fatigue 2021;145:106109.
[14] Nie B, Zhang Z, Zhao Z, Zhong Q. Effect of anodizing treatment on the very high cycle fatigue behavior of 2A12-T4 aluminum alloy. Mater Des 2013;50:1005–10.
[15] Liu X, Sun C, Hong Y. Effects of stress ratio on high-cycle and very-high-cycle fatigue behavior of a Ti–6Al–4V alloy. Mater. Sci. Engng., A 2015;622:228–35.
[16] Ding MC, Zhang YL, Lu HT. Fatigue life prediction of TC17 titanium alloy based on micro scratch. Int J Fatigue 2020;139:105793.
[17] Ritchie RO, Boyce BL, Campbell JP, Roder O, Thompson AW, Milligan WW. Thresholds for high-cycle fatigue in a turbine engine Ti–6Al–4V alloy. Int J Fatigue 1999;21:653–62.
[18] Ding J, Hall RF, Byrne J, Tong J. Fatigue crack growth from foreign object damage under combined low and high cycle loading. Part I: Experimental studies. Int J Fatigue 2007;29(7):1339–49.
[19] Gao J, Pan X, Han J, Zhu S, Liao D, Li Y, et al. Influence of artificial defects on fatigue strength of induction hardened S38C axles. Int J Fatigue 2020;139:105746.
[20] Gao J, Dai G, Li Q, Zhang M, Zhu S, Correia JAFO, Lesiuk G, De Jesus AMP. Fatigue assessment of EA4T railway axles under artificial surface damage. Int J Fatigue 2021;146.
[21] Zhang J, Li H, Yang B, Wu B, Zhu S. Fatigue properties and fatigue strength evaluation of railway axle steel: Effect of micro-shot peening and artificial defect. Int J Fatigue 2020;132:105379.
[22] Schönbauer BM, Mayer H. Effect of small defects on the fatigue strength of martensitic stainless steels. Int J Fatigue 2019;127:362–75.
[23] Kevinsanny, Okazaki S, Takakuwa O, Ogawa Y, Okita K, Funakoshi Y, et al. Matsunaga, Effect of defects on the fatigue limit of Ni-based superalloy 718 with different grain sizes. Fatigue Fract Eng Mater Struct 2019;42(5):1203–13.
[24] Wu Z, Wu S, Zhang J, Song Z, Hu Y, Kang G, et al. Defect induced fatigue behaviors of selective laser melted Ti-6Al-4V via synchrotron radiation X-Ray tomography. Acta Met Sin 2019;55:811–20.
[25] Hu Y, Wu S, Withers PJ, Zhang J, Bao HYX, Fu YN, et al. The effect of manufacturing defects on the fatigue life of selective laser melted Ti-6Al-4V structures. Mater Des 2020;192:108708.
[26] Murakami Y. Metal fatigue: effects of small defects and nonmetallic inclusions. Academic Press; 2019.
[27] Hu Y, Wu S, Wu Z, Zhong X, Ahmed S, Karabal S, et al. A new approach to correlate the defect population with the fatigue life of selective laser melted Ti-6Al-4V alloy. Int J Fatigue 2020;136:105584.
[28] Beretta S, Romano S. A comparison of fatigue strength sensitivity to defects for materials manufactured by AM or traditional processes. Int J Fatigue 2017;94:178–91.
[29] Pan X, Xu S, Qian G, Nikitin A, Shanyavskiy A, Palin-Luc T, et al. The mechanism of internal fatigue-crack initiation and early growth in a titanium alloy with lamellar and equiaxed microstructure. Mater Sci Eng A 2020;798:140110.
[30] Su H, Liu X, Sun C, Hong Y. Nanograin layer formation at crack initiation region for very-high-cycle fatigue of a Ti–6Al–4V alloy. Fatigue Fract Engng Mater Struct 2017;40(6):979–93.
[31] Sun C, Chi W, Wang W, Duan Y. Characteristic and mechanism of crack initiation and early growth of an additively manufactured Ti-6Al-4V in very high cycle fatigue regime. Int J Mech Sci 2021;205:106591.
[32] Jiang Q, Sun C, Liu X, Hong Y. Very-high-cycle fatigue behavior of a structural steel with and without induced surface defects. Int J Fatigue 2016;93:352–62.
[33] Härkegård G, Halleraker G. Assessment of methods for prediction of notch and size effects at the fatigue limit based on test data by Böhm and Magin. Int J Fatigue 2010;32(10):1701–9.
[34] Lukas P, Kunz L. Effect of mean stress on short crack threshold. Short Fatigue Cracks. 1990:265–75.
[35] Frost NE. A Relation between the critical alternating propagation stress and crack length for mild steel. Proc Inst Mech Eng 1959;173(1):811–36.
[36] Usami S, Shida S. Elastic-plastic analysis of the fatigue limit for a material with small flaws. Fatigue Fract Eng Mater Struct 1979;1:471–81.